Check for updates

Plasmene nanosheets assembled from "plasmonic molecules"

Qianqian Shi, †*[a] Bo Fan, †[b] Xiaorui Cao, †[c] Debabrata Sikdar, [d] Yifeng Huang, [e] Jialiang Yin, [e] Yan Lu, [c] San H. Thang [b] and Wenlong Cheng *[c]

Entropy-driven drying-mediated self-assembly of plasmonic nano-crystals (termed "plasmonic atoms") has emerged as a general strategy for fabricating plasmene nanosheets from a wide range of monodisperse nanocrystals. However, extending this approach to binary systems remains challenging due to the complex nanoscale interactions between dissimilar nanocrystal shapes. Here, we introduce a combined enthalpy- and entropy-driven strategy to achieve an orderly mixed two-dimensional (2D) binary nanoassemblies from complementary reacting polymer-ligated nanocrystals. Using nanocubes and nanospheres as model systems, "plasmonic molecules" were first synthesized *via* enthalpy interactions of different nanocrystals through stoichiometric reactions between complementary grafting polymers. This was followed by an entropy-driven, slow-drying-mediated assembly of "plasmonic molecules". This led to well-controlled binary plasmenes without phase separation. This method could be extended to a diverse range of other building block shapes and size scales. Our methodology indicates a new pathway for 2D nanocrystal assemblies with well-controlled mixing at nanoscale precision.

New concepts

This work presents a novel concept of assembling binary plasmenes using 'plasmonic molecules' as the fundamental building blocks. Unlike traditional self-assembly methods for plasmene nanosheets (two-dimensional plasmonic nanoassemblies) formed from individual nanoparticles, our approach employs binary plasmonic molecules composed of dissimilar nanoparticles. This strategy effectively mitigates phase separation caused by differences in nanoparticle size and structure, enabling the formation of well-mixed nanoassemblies from a wide variety of nanoparticles. Our research also reveals that the nanoparticles undergo a rearrangement during a slow-drying, entropy-driven process, providing new insights into the mechanisms of self-assembly. Furthermore, our method offers flexibility in tuning the binary plasmene system through various parameters, including polymer concentration, polymer length, and nanoparticle ratio. This opens new avenues for the co-assembly of artificial atoms with tailored structures and properties which are difficult to achieve using conventional entropy-driven self-assembly techniques.

Introduction

Nanoparticle assembly provides a direct and powerful strategy to control the properties of nanomaterials by tuning interparticle interactions and enabling collective behaviors that differ significantly from those of individual nanoparticles. Binary assemblies further expand the capabilities of nanoparticle self-assembly by combining the properties and structures of two distinct building blocks.[1–8] These binary nanoassemblies have demonstrated unique magnetic, optical, and structural characteristics that are difficult to achieve with single-component systems. For example,

free-standing two-dimensional binary nanoassemblies fabricated from Fe_3O_4 and FePt nanocrystals have exhibited tunable magnetoresistance.[8] Binary superlattices self-assembled from CdSe and Au nanocrystals demonstrated tunable fluorescence properties.[5] Different types of 2D binary nanocrystal superlattices, including some structures not previously reported, were fabricated from Au and Fe_3O_4 nanocrystals.[4] However, success in this area has been largely limited to spherical nanoparticles with typical dimensions below 20 nm. Extending such approaches to fabricate binary systems using building blocks in the medium- to large-sized nanoscale range, as well as non-spherical nanoparticles, remains challenging due to the complex nanoscale forces involved in the kinetic self-assembly process and the relatively small size of most molecular ligands compared to the larger dimensions of these nanoparticles.[9,10]

[a] *School of Environmental and Life Sciences, University of Newcastle, Callaghan 2308, New South Wales, Australia. E-mail: qianqian.shi@newcastle.edu.au*
[b] *School of Chemistry, Monash University, Clayton 3800, Victoria, Australia*
[c] *School of Biomedical Engineering, University of Sydney, Darlington 2008, New South Wales, Australia. E-mail: wenlong.cheng@sydney.edu.au*
[d] *Department of Electronics and Electrical Engineering, Indian Institute of Technology Guwahati, Guwahati, 781039, Assam, India*
[e] *Department of Chemical & Biological Engineering, Faculty of Engineering, Monash University, Clayton 3800, Victoria, Australia*
† These authors contributed equally.

On the other hand, significant progress has been made to synthesize plasmonic nanoparticles with controlled compositions, shapes, and sizes, forming the so-called artificial periodic table of plasmonic atoms.[11] Further success has been reported to synthesize "plasmonic molecules" by using DNA-directed[12–21] and polymer-based approaches,[22–28] and three-dimensional (3D) plasmonic crystal DNA-directed strategies.[29–33]

It has also been demonstrated that two-dimensional (2D) ordered assemblies of plasmonic atoms (or plasmene) could be rationally fabricated from >15 different nanocrystals in a drying-mediated self-assembly approach.[34] Such 2D plasmene nanosheets emerge as a new class of advanced materials, demonstrating novel applications in sensing,[35–39] encryption,[40] nanophononics,[41] ionic gating,[42] and photocatalysis.[43–46] Despite these advances, current success was limited to single-component systems. Binary plasmonic nanoassemblies open a new frontier for engineering plasmonic coupling and bandgap modulation. For example, binary nanoassemblies composed of Au nanocubes (NCs) and Au@Ag NCs of similar dimensions have demonstrated controllable collective plasmonic properties by precisely adjusting the ratio between two building blocks, exhibiting n-type and p-type-like plasmonic properties analogous to those in semiconductors.[47] However, it has been challenging to extend the aforementioned drying-mediated, entropy-driven approach to fabricate binary plasmenes from different shaped nanoparticles due to complex nanoscale forces among structurally dissimilar nanocrystal building blocks.[10]

Here, we report a new strategy to fabricate binary plasmenes *via* a combined enthalpy and entropy process. Unlike previous plasmonic nanoassemblies that are directly assembled from individual nanoparticles ("atoms"), this approach involves first fabricating artificial "plasmonic molecules" from plasmonic atoms through enthalpy complementary interacting polymeric ligands, followed by assembling these artificial molecules into plasmenes in an entropy-driven self-assembly process. The tunable polymer length and the stoichiometric interactions between complementary grafted polymers allow controlling the structure of the plasmonic artificial molecules and effectively mitigating phase separation caused by differences in nanoparticle size and structure, enabling the formation of well-mixed nanoassemblies from size and structural dissimilar nanoparticles. Using Au nanospheres (NSs) and NCs as a model system, we demonstrate the formation of binary plasmene assemblies without any phase separation. We also revealed a rearrangement of the nanoparticles during the slow-drying process, leading to well-mixed, closely-packed binary assemblies that are difficult to achieve using conventional entropy-driven methods. This strategy is general and extendable to different binary systems, including nanobipyramids (NBPs) and NCs, NBPs and NSs, and NSs and nanorods (NRs) in the medium to large nanoscale range – the dominant size range represented in the artificial periodic table, offering a general design rule applicable to a variety of building block shapes and opening new strategies for designing metal nanomaterials with combined properties.

Results and discussion

We began with structurally dissimilar Au NSs and NCs as the model system. Both colloidal Au NSs and NCs were synthesized using the seed-mediated growth method.[47,48] Transmission electron microscopy (TEM) and scanning electron microscopy (SEM) imaging (Fig. S1) revealed that the Au NSs had an average diameter of 23.6 ± 0.7 nm, while the Au NCs had an edge length of 52.9 ± 2.1 nm. These dimensions were selected to enable a maximum of two NSs to attach to each face of a NC.

A two-step enthalpy–entropy self-assembly strategy was employed to fabricate the binary plasmene. To initiate
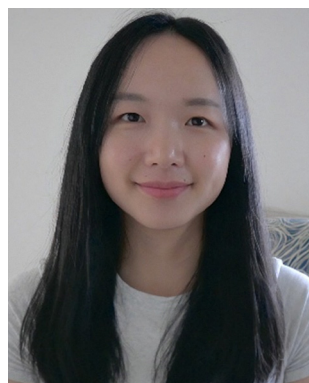
Qianqian Shi

Qianqian Shi: I am honoured to contribute to the 10th anniversary issue of Nanoscale Horizons. Since 2018, I have actively engaged with the journal, publishing several collaborative papers on electronic skin, optical skin strain sensors, novel plasmonic nanocrystals, and wearable biosensors. In 2023, I was fortunate to join the Community Board. As I transition from an early to mid-career researcher, I greatly value the opportunity to showcase our recent research through this respected platform. Congratulations to Nanoscale Horizons on its 10th anniversary; I look forward to continuing our contributions and to the journal's ongoing impactful role in advancing the field of nanoscience.

Wenlong Cheng

Wenlong Cheng: Congratulations to Nanoscale Horizons on reaching its 10th anniversary. It has been a privilege to contribute to the journal both as a Scientific Editor and as an author, with four of my articles published in this flagship Royal Society of Chemistry journal. I have also had the pleasure of contributing three research articles to its sister journal, Materials Horizons. My research focuses on the self-assembly of two-dimensional plasmonic nanomaterials, DNA nanotechnology, electronic skins, and wearable bioelectronics. I look forward to contributing to the continued success of Nanoscale Horizons in shaping the field of modern nanoscience and nanotechnology over the next decade and beyond.

enthalpy-driven binary "plasmonic molecule" formation, Au NSs and NCs were functionalized with thiol-terminated polystyrene-*block*-poly(styrene-*random*-acrylic acid) (PS-*b*-P(S-*r*-AA)-SH) and thiol-terminated poly(ethylene oxide)-*block*-poly(*N*,*N*-dimethylaminoethyl methacrylate-random-styrene) (PEG-*b*-P(S-*r*-DMAEMA)-SH), respectively, *via* a two-step ligand exchange procedure (Fig. 1(a)). These complementary copolymer ligands enable controlled interactions between the two particle types through a stoichiometry-driven process.[22] After functionalization, both types of nanocrystals remained well-dispersed, showing no visible color change (Fig. S2a–d) or wavelength shift in their ultraviolet-visible (UV-vis) spectra (Fig. S2e) even after ten washing cycles, confirming successful polymer grafting.

The ligands on Au nanocrystals are expected to form a polymer brush layer that provides sufficient reactive groups for subsequent bonding reactions. To prove this, Au NSs capped with 0.5 mg mL^{-1} PS-*b*-P(S-*r*-AA)-SH were analyzed using dynamic light scattering (DLS, Fig. S3a) and TEM (Fig. S1a) across various polymer molecular weights (M_n). The brush height was estimated by subtracting the NS core size determined by TEM from the hydrodynamic diameter obtained *via* DLS, and the resulting values were plotted against M_n. As shown in Fig. S3b, the scaling exponent between the brush height and M_n was found to be 0.62, consistent with a polymer brush regime on the NS surface.[4] Given that the surface area of the NC is approximately twice that of the NS, a higher polymer concentration (1 mg mL^{-1}) was used to modify Au NCs.

The copolymer-functionalized NSs and NCs were then combined and left undisturbed for 2 hours, allowing enthalpy-driven assembly through electrostatic neutralization between the oppositely charged polymers, resulting in the formation of binary "plasmonic molecules" (Fig. 1(b)). These preassembled "plasmonic molecules" were then used as building blocks for a second self-assembly step, in which a concentrated solution of the "plasmonic molecules" was deposited onto a water droplet surface and assembled *via* the entropy-driven air–water interfacial self-assembly method (Fig. 1(c)).[34,49] The resulting binary plasmene formed a continuous film with a distinct purple color in a transmission mode (Fig. 1(d)). SEM imaging revealed that the assemblies possessed high microscale uniformity, with Au NSs and NCs well-distributed and no observable phase separation at either the micro- or nanoscale (Fig. 1(e)).

To highlight the important role of interactions between oppositely charged polymers, a control experiment was conducted in which both building blocks were grafted with the same ligand. Specifically, both NSs and NCs were grafted with the same polymer PS-*b*-P(S-*r*-AA)-SH and then mixed and concentrated before being deposited onto the surface of a water droplet following the same entropy-driven self-assembly method as mentioned above (Fig. 1(f)–(g)). Due to the size mismatch and structural difference between the nanocrystals and the absence of directional interactions to mediate the incompatibility between domains, phase separation occurred in the obtained binary assemblies (Fig. 1(h) and Fig. S4a). There are even some regions where NCs are not surrounded by any NSs (Fig. S4b).

In another control experiment, a binary plasmene was fabricated by directly mixing the complementary NSs and NCs, followed by immediate deposition of the mixture onto the water surface without the 2 hour reaction time (Fig. 1(i) and (j)). While this strategy successfully prevented phase separation, the resulting assembly was discontinuous and exhibited a poor structural order, with noticeable aggregates, voids, and a random distribution of NSs around NCs (Fig. 1(k) and Fig. S5), highlighting the critical role of plasmonic molecule formation in controlling binary assembly quality.

Unlike the traditional assembly process, in which individual nanoparticles serve as the building blocks, in this work, binary plasmonic molecules were employed as the fundamental units for subsequent assembly. The SEM image confirmed the "plasmonic molecule" structure from the binary solution that was collected after 2 hours of reaction (Fig. 2(a)). The original colloidal solution of NSs exhibited a peak at 527 nm, while the NCs displayed a peak at 538 nm. The binary mixture displayed a red shift relative to both the NS and NC solutions (Fig. 2(b)), indicating coupling interactions between NCs and NSs within the "plasmonic molecules".

Since the solvent evaporation kinetics affect the self-assembly of nanoparticles,[8] the assembly system was further exposed to chloroform vapor and covered with a glass lid to facilitate vapor-assisted slow-drying (Fig. 2(c)) and allow sufficient time for interactions between the "plasmonic molecules". The final binary assemblies were collected after the water droplet had completely evaporated. The resulting binary assemblies displayed a distinct blue color in transmission mode under a microscope, with the color uniformly distributed over areas spanning hundreds of micrometers on the ITO glass, indicating high uniformity (Fig. 2(d)). SEM images (Fig. 2(e)) revealed a more uniform and closely packed structure compared to the normal-drying process, indicating that slow-drying is an effective method for enhancing enthalpic interactions between complementary ligand groups and improving the overall quality of the binary plasmene. The resulting binary assemblies exhibited mixed Au NC : Au NS ratios of 1 : 2 and 1 : 3 (referred to as BF$_2$-like and BF$_3$-like structures, respectively), which are close to the theoretical feeding ratio of 1 : 2.5.

The different packing densities had a pronounced impact on the plasmonic properties of the binary plasmene. The average interparticle distance in the normal-dried binary plasmene was 35.8 ± 8.4 nm, whereas the slow-dried plasmene exhibited a reduced distance of 28.2 ± 6.6 nm. As shown in Fig. 2(f), both types of plasmene displayed red-shifted peaks relative to the original binary solution, indicating enhanced plasmonic coupling between nanocrystals. Notably, the slow-dried plasmene exhibited an additional red shift of 16.1 nm compared to the normal-dried sample, attributed to the decreased interparticle spacing. Furthermore, a distinct peak emerged in the near-infrared (NIR) region for the normal-dried plasmene (red curve, Fig. 2(f)).

Our simulation results suggest that the plasmonic modes in these two types of plasmenes arise from different types of nanoparticle arrangements. In the normal-dried plasmene,
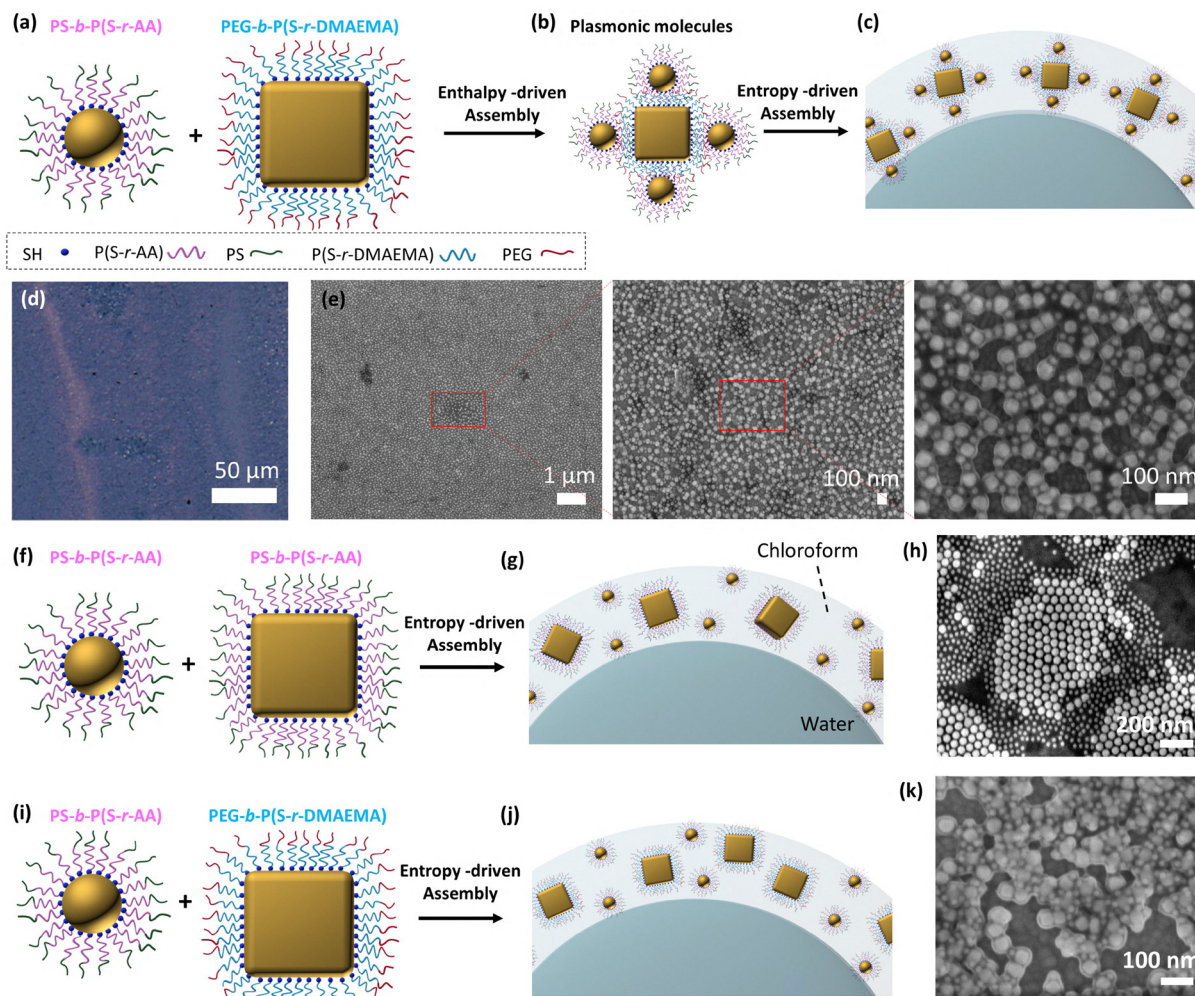
Fig. 1 Self-assembly of binary plasmene. Schematic illustration of (a) PS-*b*-P(S-*r*-AA)-SH-functionalized Au NSs and PEG-*b*-P(S-*r*-DMAEMA)-SH-functionalized Au NCs, (b) binary ''plasmonic molecules'', (c) self-assembly of ''plasmonic molecules'' at the air−water interface, and the corresponding (d) transmission optical image and (e) SEM images of the obtained binary plasmene at different magnifications. (f) Schematic illustration of PS-*b*-P(S-*r*-AA)-SH capped Au NSs and PS-*b*-P(S-*r*-AA)-SH capped Au NCs, (g) their self-assembly on the air−water interface, and the (h) corresponding SEM image of binary plasmene. (i) Schematic illustration of PS-*b*-P(S-*r*-AA)-SH capped-Au NSs and PEG-*b*-P(S-*r*-DMAEMA)-SH-capped-Au NCs, (j) their self-assembly on the air−water interface without the 2 hour reaction time, and the (k) corresponding SEM image of binary plasmene.

Au NSs are not uniformly distributed among the NCs, leading to two predominant structural motifs: (i) mode 1 (58%): one or two NSs positioned between adjacent NCs and (ii) mode 2 (42%): two NCs in proximity with each other. These two configurations primarily contributed to a strong absorbance peak at around 600 nm (Fig. 2(g)). In mode 2, additional peaks were observed between 700 and 800 nm and in the NIR region (900–1000 nm). In contrast, the slow-dried plasmene exhibited more ordered structures. Two representative configurations were identified based on the number of NSs surrounding each NC. A unit containing eight NSs produced a strong absorbance peak at around 609 nm, while a unit with six NSs showed a peak at 604 nm. Both configurations generated a single dominant peak in the visible region (Fig. 2(h)), contributing to the one main peak in Fig. 2(f) (blue curve). For the pronounced peak at around 1000 nm observed in the normal-dried sample, our

simulations indicate strong coupling between NCs within dimeric and trimeric aggregates (Fig. S6). The plasmon excitation along the longitudinal axis of these dimers and trimers produces a dominant broad peak near 950 nm, which is consistent with the higher degree of NC–NC contacts in the normal-dried sample (Fig. 1(e)) compared to the slow-dried sample (Fig. 2(e)).

We also noticed that in the binary plasmene formed under the slow-drying conditions, the original BF_2-like and BF_3-like structures of the binary molecules were not preserved during assembly, suggesting that a nanocrystal rearrangement occurred during the slow-drying process. Based on the difference in density between the slow- and normal drying processes, this rearrangement likely involved in-plane repositioning and movement, particularly of NSs and NCs initially adjacent to one another. For example, interactions between the complementary
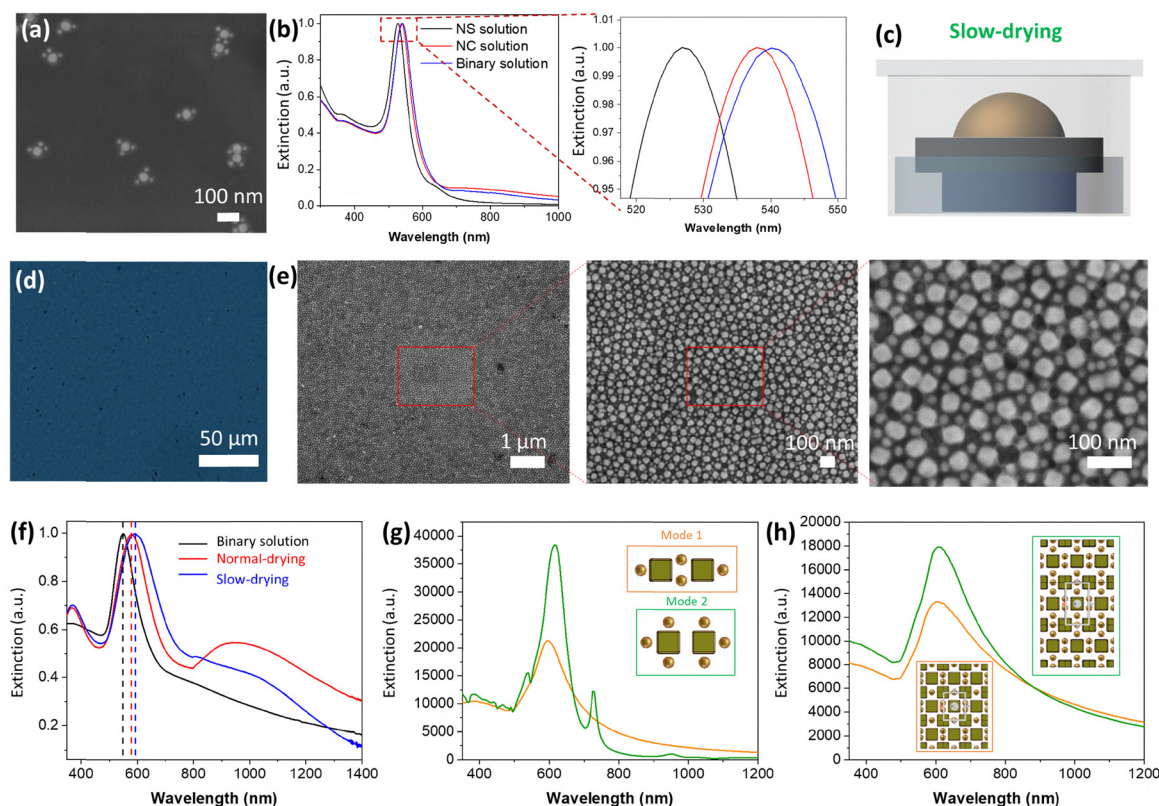
Fig. 2 Optimizing the binary plasmene structure by introducing a slow-drying process. (a) SEM image of "plasmonic molecules" with a feeding ratio of NC : NS = 1 : 2.5. (b) Comparison of the plasmonic peaks from Au NS colloidal solution (black curve), Au NC colloidal solution (red curve), and the plasmonic binary molecules solution (blue curve). (c) Schematic illustration of the slow-drying self-assembly, and the corresponding (d) transmission optical image. (e) SEM images of the obtained binary plasmene at different magnifications. (f) Comparison of the plasmonic peaks from the binary plasmonic molecule solution (black curve), and the binary plasmene from normal-drying self-assembly (red curve), and binary plasmene from slow-drying self-assembly (blue curve). Theoretical simulations of the plasmonic properties of binary assemblies from (g) normal-drying self-assembly and (h) slow-drying self-assembly.

polymers drive nearby NSs from molecule A and NCs from molecule B to move closer together, leading to NS reorganization and a more closely packed arrangement compared to the initial state (Fig. 3(a)). SEM and atomic force microscopy (AFM) analyses confirmed a monolayered structure in the final assemblies (Fig. 3(b)–(d)). Cross-sectional imaging revealed that some NSs were even vertically displaced above other NSs along the z-axis in specific regions (Fig. 3(c)).

To further investigate this rearrangement process, samples dried under different time intervals during a slow-drying process were examined by SEM. The assemblies transitioned from a loosely packed to a closely packed structure over a period of 0 to 6 hours and maintained this compact structure up to 30 hours (Fig. 3(e) and Fig. S7). By measuring interparticle distances, we found that the NC–NC spacing decreased from 95.5 ± 19.5 nm at 0 hours to 84.3 ± 12.8 nm and 85.4 ± 13.7 at 6 hours and 8 hours, respectively, remaining stable thereafter (Fig. 3(f), black squares), consistent with SEM observations. In contrast, the NC–NS distance remained relatively constant at approximately 33 nm, suggesting that while the NSs underwent local rearrangement during drying, the overall structure of the binary "plasmonic molecules" was maintained (Fig. 3(f),

red triangles). This structural rearrangement was further supported by the shifts in the plasmonic peak positions (Fig. 3(g)), which show that the binary assemblies exhibited a red shift from an initial peak at 582 nm to 588 nm at 6 hours, with the peak position remaining stable up to 30 hours.

To further investigate the structural rearrangements in the binary assemblies during self-assembly, a Voronoi analysis was performed to determine the spatial distribution of the plasmonic molecules within the nanoassemblies. This analysis was conducted on the SEM images using the NCs as central reference points (Fig. S8). The distribution of the number of polygon edges is summarized in Fig. 3(h). Notably, irregular hexagons dominated the self-assembly structures, with over 40% of the polygons being hexagons at 0 hours. Their proportion increased with drying time, while the fractions of quadrilateral and octagonal polygons decreased to zero after 8 hours. Given that each binary molecule is centered at an NC, this suggests a predominant hexagonal arrangement of the binary molecules. In a control experiment, no significant differences were observed between the normal- and slow-drying samples for NC-only and NS-only systems without complementary ligands (Fig. S9), further supporting that the
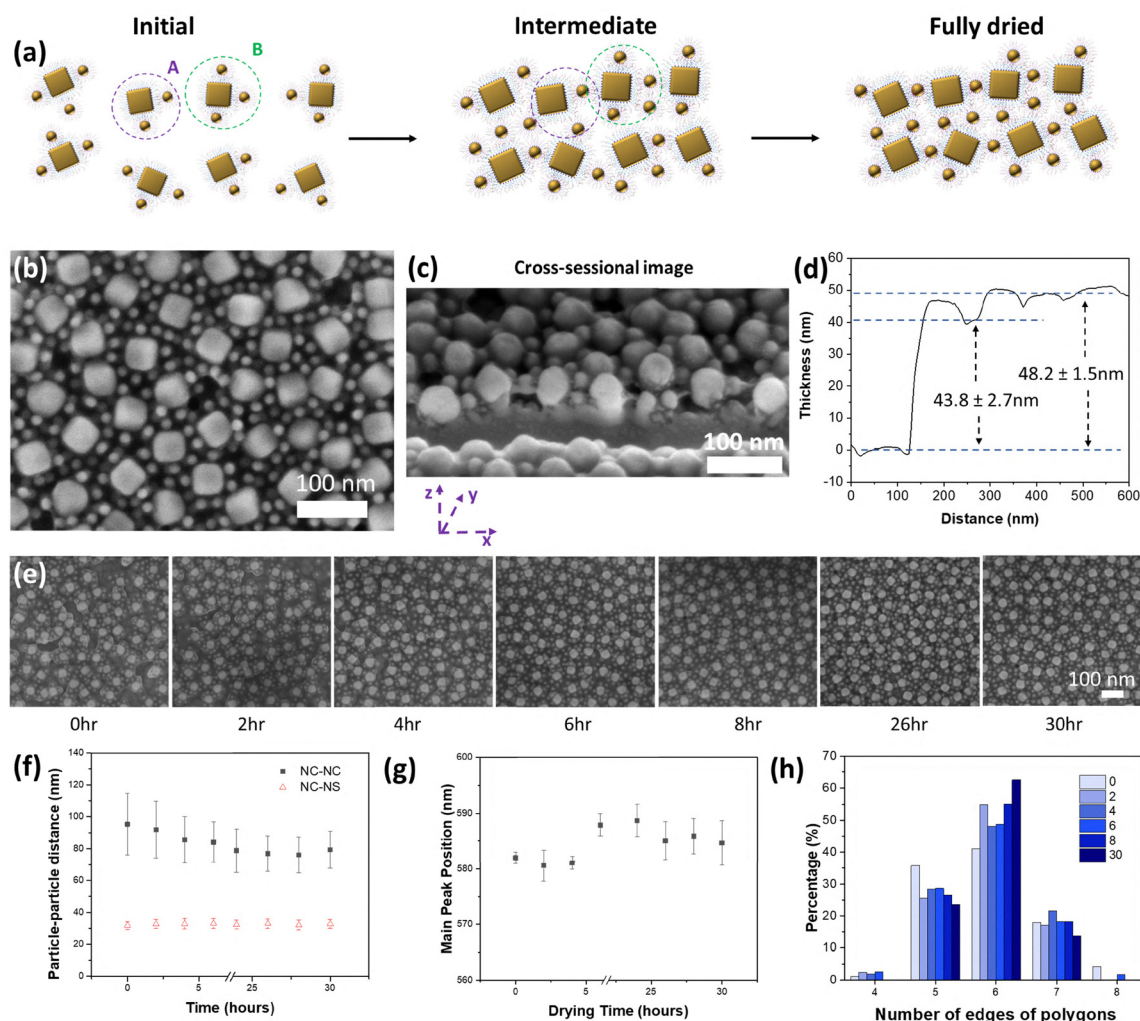
Fig. 3 Nanocrystal reorganization during the slow-drying self-assembly. (a) Schematic illustration showing the proposed self-assembly process of binary "plasmonic molecules" at the air–water interface at the initial, intermediate, and fully dried states. SEM images of a fully dried binary plasmene from slow-drying at (b) top and (c) cross-sectional views. (d) AFM of a monolayered binary plasmene. (e) Time-resolved evolution of the binary plasmene at 0, 2, 4, 6, 8, 26, and 30 h from SEM images. (f) The interparticle distance change and (g) the main peak position change from binary plasmene collected at different time points. The interparticle distances were determined by measuring the center-to-center distances between NC–NC and NS–NS pairs in the SEM images. For each sample, 178–286 NC–NS pairs and 208–480 NC–NC pairs were measured. (h) The percentage of different types of polygons from the Voronoi analysis.

rearrangement in the binary system under slow-drying conditions was driven by complementary ligand interactions.

Since the interactions between nanocrystals are primarily driven by polymers, we also investigated the effect of polymer length (polymers with different molecular weights M_n) on the binary assemblies. Given that the rearrangement mainly occurs in the NSs, we varied the polymer length of PS-*b*-P(S-*r*-AA)-SH on the NSs for fabrication of binary plasmenes. As shown in Fig. 4(a)–(d) and Fig. S10, binary plasmenes were successfully formed across all samples. In the plasmene with shorter polymer lengths, the NSs tended to aggregate in localized regions (Fig. 4(a) and Fig. S10a), likely due to the stronger van der Waals forces associated with shorter polymer ligands. As the PS-*b*-P(S-*r*-AA)-SH length increased, the binary assemblies displayed more uniform arrangements (Fig. 4(b)–(d) and Fig. S10b–d).

To better visualize the spatial distribution and structural evolution of the NSs, we pseudo-colored the NCs and NSs differently in Fig. S11.

UV-vis absorbance spectra confirmed that as the polymer length increased, the main absorption peak red-shifted from 597 nm to 617 nm and 607 nm for the 12k, 18k, and 30k samples, respectively (Fig. 4(e)). Interestingly, for the 55k PS-*b*-P(S-*r*-AA)-SH sample, the peak exhibited a blue shift compared to the 18k and 30k samples, which can be attributed to the increased spacing between NCs. However, the 55k PS-*b*-P(S-*r*-AA)-SH sample also exhibited a significantly sharper peak, indicating a more uniform structural arrangement. To further quantify the structural differences, we performed Voronoi analysis centered on the NCs within the binary assemblies (Fig. 4(f)–(i)). For the 12k PS-*b*-P(S-*r*-AA)-SH sample, the
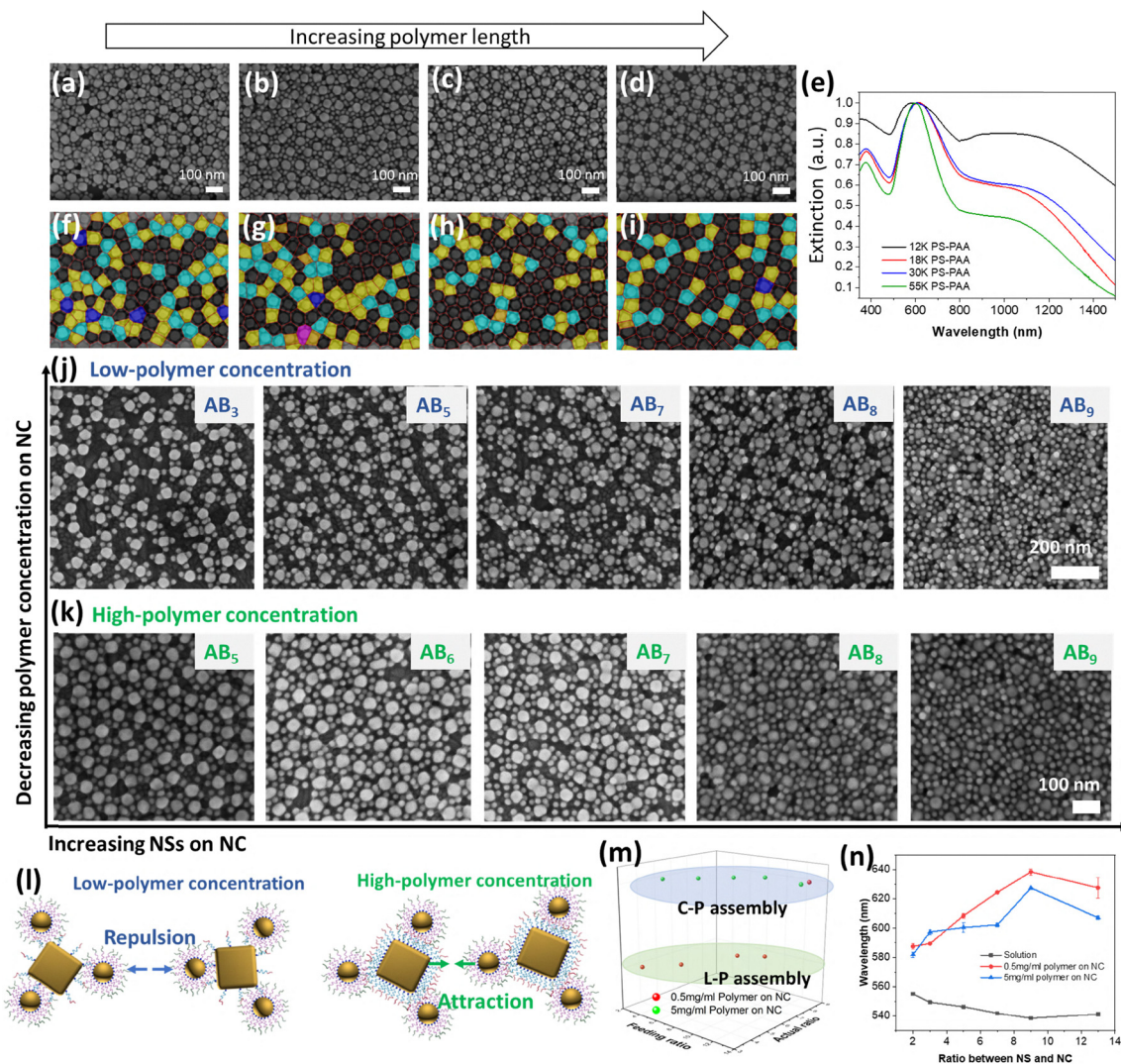
Fig. 4 The effect of the polymer length, concentration and feeding nanocrystal ratio on the binary plasmene. SEM images of the binary plasmene assembled from different PS-*b*-P(S-*r*-AA)-SH polymer lengths of (a) 12k, (b) 18k, (c) 30k and (d) 55k. (e) Comparison of the plasmonic peaks of the binary plasmene from different lengths of PS-*b*-P(S-*r*-AA)-SH. (f)–(i) Voronoi analysis of the binary plasmenes. SEM images of the binary plasmene from different feeding ratios between NCs and NSs of 1:3, 1:5, 1:7, 1:9, and 1:13 at (j) a low (0.5 mg ml⁻¹) and (k) a high (5 mg ml⁻¹) concentration of the PEG-*b*-P(S-*r*-DMAEMA)-SH polymer. The ABx in the image represents the actual NC and NS ratio in the binary assemblies, where x is the number of NSs per NC. (l) Proposed interactions between binary "plasmonic molecules" at low and high PEG-*b*-P(S-*r*-DMAEMA)-SH polymer concentrations on Au NCs. (m) The relationship of the feeding ratio, actual ratio, and type of assembly. (n) The main plasmonic peak wavelength changes of the binary plasmene from low and high concentrations of the polymer on the NC and the binary molecule solution.

polygonal distribution consisted of 28% pentagons, 41% hexagons, and 22% heptagons (Fig. 4(f) and Fig. S12). With increasing polymer length, the proportion of hexagons increased to 55% in the 18k sample, 64% in the 30k sample, and 56% in the 55k sample, consistent with the hexagonal arrangement in NC-only assemblies and confirming the increasing structural uniformity (Fig. S13).

Considering that the polymer concentration on NCs determines the number of available binding sites for NSs, we further investigated the effect of polymer concentration on the binary assemblies. We precisely controlled the concentration of PEG-*b*-P(S-*r*-DMAEMA)-SH on NCs, ranging from 0.1 mg mL⁻¹ to 5 mg mL⁻¹, using a theoretical feeding ratio of NC:NS = 1:2.5 (Fig. S14). At both the

lowest and the highest polymer concentrations, each NC was typically surrounded by 2 or 3 NSs in the "plasmonic molecules". In contrast, at intermediate concentrations of 0.5 mg mL⁻¹ and 1 mg mL⁻¹, most NCs were mainly surrounded by 3 NSs (Fig. S14). These four types of binary molecules were then assembled into 2D monolayered plasmenes using the slow-drying assembly method, which exhibited a distinct blue color in transmission mode and a red-shifted plasmonic peak compared to their binary solutions (Fig. S15a and S16). All samples demonstrated uniformity across hundreds of micrometers, except the film formed from the lowest polymer concentration, likely due to weaker interactions between adjacent binary molecules (Fig. S15a). At the nanoscale, this sample also displayed a more loosely packed and less ordered structure

compared to the others (Fig. S15b). For the remaining three samples, the effect of PEG-*b*-P(S-*r*-DMAEMA)-SH concentration on the assembly structure was less pronounced.

To further investigate the effects of polymer ligand concentration and particle ratio on the binary assemblies, we used two concentrations of PEG-*b*-P(S-*r*-DMAEMA)-SH on the NCs: 0.5 mg mL^{-1} and 5 mg mL^{-1} for the binary assemblies. For each polymer ligand concentration, we also varied the feeding ratio of NCs to NSs by adjusting their respective volumes. At the lower polymer concentration (Fig. 4(j)), the binary assemblies tended to form loosely packed structures, where individual binary molecules were positioned close to one another but remained separated. As the feeding ratio of NCs to NSs increased from 1:3 to 1:5, 1:7, 1:9, and 1:13, the corresponding NC:NS ratios in the resulting binary assemblies were approximately 1:3, 1:5, 1:7, 1:8, and 1:9, respectively. These values were very close to the feed ratio and were labeled as AB$_3$, AB$_5$, AB$_7$, AB$_8$, and AB$_9$. Notably, the binary assemblies appeared to reach saturation at a ratio of 1:9 (AB$_8$), beyond which further increases in the NS concentration (*e.g.*, at a 1:13 feeding ratio) led to the formation of multilayered structures.

In contrast to the binary assemblies formed at low polymer concentrations, higher polymer concentrations resulted in more uniform and closely packed assemblies (Fig. 4(k)). With a greater amount of polymer on the NC, the actual ratio of NC to NS increased compared to the lower concentration samples, even when the feeding ratio remained the same. Similar to the lower polymer concentration samples, the binary system from a higher polymer concentration also reached saturation at a ratio of 1:9. However, instead of forming multiple aggregated NSs on the NCs, the binary samples at a feeding ratio of 1:13 formed a monolayered and uniform structure.

The schematic illustration in Fig. 4(l) proposes the mechanism of the binary molecule assembly process at high and low concentrations of the polymer on NCs. At lower polymer concentrations, limited bonding sites are available on the NCs, restricting the attraction between NCs and NSs in adjacent binary molecules. Consequently, the interactions between binary molecules are dominated by repulsive forces between NSs, resulting in loosely packed assemblies with individual binary molecules on the substrate. In contrast, at higher polymer concentrations, the available sites on the NCs not only provide connections to the NSs within the same binary molecules but also facilitate interactions with NSs from adjacent molecules, leading to stronger interactions between the NC and any nearby accessible NSs, resulting in more closely packed assemblies. As a result, low polymer concentrations lead to loosely packed (L-P) assemblies, except at a feeding ratio of 1:13 (Fig. 4(m), green circular region), while all high polymer concentration samples form closely packed (C-P) assemblies (Fig. 4(m), blue circular region).

To monitor their plasmonic properties, we compared the plasmonic peaks of binary assemblies formed at low and high polymer concentrations, as well as their corresponding binary molecules in solutions. As shown in Fig. 4(n) and Fig. S17, both types of binary assemblies exhibited a red shift in their absorbance spectra compared to the binary molecules in solution,

indicating stronger plasmonic coupling between the nanocrystals. For both L-P and C-P assemblies, the peak wavelength initially increased with the feeding ratio, reaching a maximum at a saturation point of 1:9. Beyond this threshold, the peak wavelength blue-shifted, likely due to the excess NSs incorporated into the assemblies. Interestingly, the L-P assemblies exhibited a more pronounced red shift compared to the C-P assemblies across all feeding ratios, except at a 1:5 ratio. This may be caused by the presence of overlapping thick polymer layers in the high-polymer-concentration samples, which provide more interaction sites for the NS but also increase the spacing between nanoparticles.

This method is generalizable and can be applied to a variety of binary assemblies composed of different anisotropic nanocrystals. To demonstrate this, we prepared binary plasmenes using Au NBP and NC (Fig. 5(a)), NBP and NS (Fig. 5(b)), and NR and NS (Fig. 5(c)). The plasmonic spectra of the binary solutions exhibited distinct peaks that combined the characteristic features of each individual nanocrystal type (Fig. 5(d)–(f)). In particular, the main peaks from binary molecule solution composed of NBP and NC showed a more pronounced red shift compared to their individual nanocrystal solutions, which may be caused by closer contact between the facets of the NC and NBP relative to the other two systems. Upon assembly, the binary structures retained these properties, but showed red-shifted absorbance peaks compared to their plasmonic molecule solution counterparts, indicating enhanced plasmonic coupling between nanocrystals in the assembled state. Interestingly, the plasmonic peak shifts of identical nanocrystals varied across different binary systems, indicating system-dependent coupling effects. For instance, the peak corresponding to NBP red-shifted by 46 nm in the NBP + NC system, while a larger shift of 131 nm was observed in the NBP + NS system. Similarly, the NS peak red-shifted by 62 nm in the NBP + NS system, compared to a 32 nm shift in the NR + NS system. These results suggest varying plasmonic coupling strengths arising from different structural features, such as tip-to-NS interactions in the NBP + NS system and facet-to-NS interactions in the NR + NS system, which are difficult to observe in single-component systems. Additionally, new plasmonic peaks emerged at around 400 nm in all binary systems, indicating the formation of new plasmonic coupling modes. Together, these findings demonstrate that our approach to binary assembly provides a flexible platform for tuning the optical properties of the assemblies across a broad spectral range and introducing new plasmonic modes, without compromising their structural uniformity.

In summary, we report a general and versatile assembly strategy for fabricating binary plasmenes from nanocrystals of various shapes. By combining enthalpy-driven "plasmonic molecules" assembly and slow-drying-mediated entropy-driven assembly, we successfully constructed uniform, close-packed binary plasmenes from multiple combinations, including NC + NS, NBP + NC, NBP + NS, and NR + NS. Using the NC + NS system as a model, we found that enthalpic acid–base interactions between functional groups on the polymer ligands effectively prevent phase separation. The uniformity of the structures can be enhanced by applying a slow-
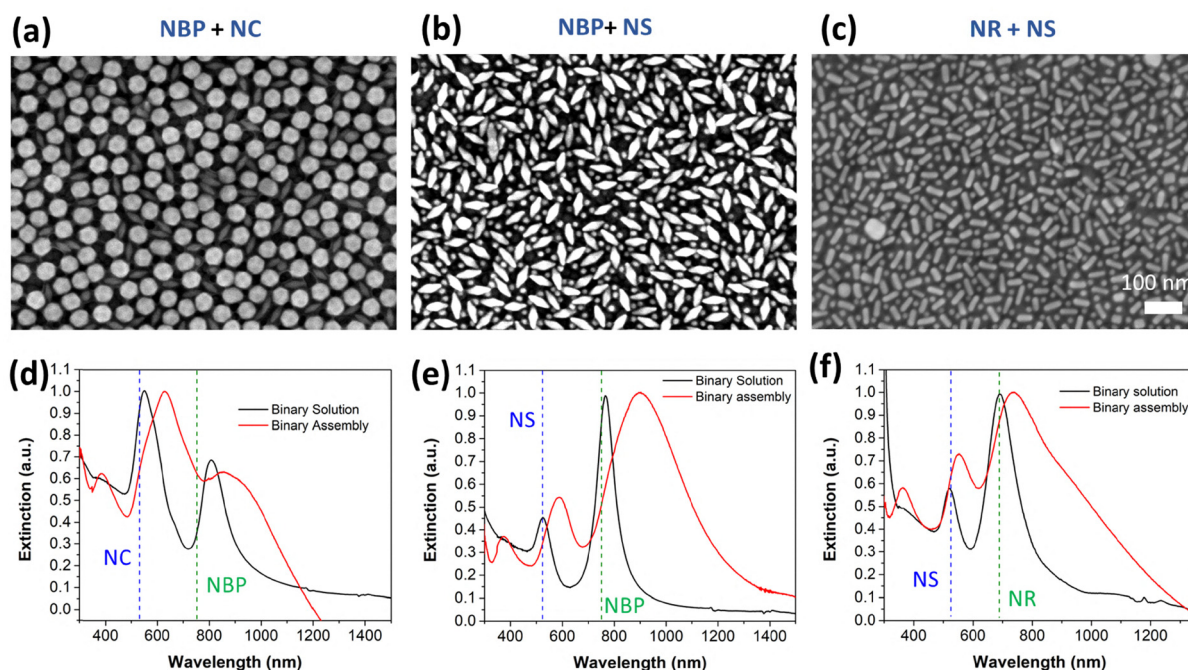
Fig. 5 Binary plasmene from different types of binary molecules. SEM images of the binary assemblies from (a) NBP (length: 50.5 ± 3.0 nm and width: 17.3 ± 1.4 nm) + NC, (b) NBP (length: 65.0 ± 3.4 nm and width: 22.5 ± 1.8 nm) + NS (13.2 ± 1.2 nm), and (c) NR (length: 44.3 ± 2.8 nm and width: 14.5 ± 1.4 nm) + NS (13.2 ± 1.2 nm). Comparison of the plasmonic properties between the binary molecule solutions and the binary plasmene from (d) NBP + NC, (e) NBP + NS, and (f) NR + NS.

drying process, during which the nanoparticle rearrangement occurs within the first six hours of assembly. In this period, NSs interact with NCs from both their original and neighboring binary units, thereby facilitating well-controlled nanoscale arrangements. By tuning the polymer length and concentration, we were able to control the assembly behavior, yielding both C-P and L-P arrangements with tunable optical properties and adjustable nanoparticle ratios. More importantly, this method offers a general strategy for designing 2D binary assemblies composed of building blocks with dissimilar shapes and sizes, enabling system-specific coupling effects and the emergence of new plasmonic modes. Given its versatility, we anticipate that it can also be applied to non-plasmonic particles (such as quantum dots, perovskite nanocrystals, magnetic particles, dielectric particles, semiconducting nanoparticles, and carbon nanoparticles), as well as to combinations of plasmonic and other metallic nanoparticles. This approach holds promising potential for designing metasurfaces with tailored optical responses, controllable hot spots, and integrated optical, catalytic, magnetic, and electronic properties, offering versatile functionality for next-generation applications in photodetectors, optical filters, metasurface lenses, optical sensors, surface-enhanced Raman scattering substrates, plasmonic waveguides, and photothermal devices.

Methods

Chemicals

Sodium borohydride (NaBH$_4$, 99.99%), L-ascorbic acid (L-AA, 99%), hexadecyltrimethylammonium bromide (CTAB, 99%),

cetyltrimethylammonium chloride solution (CTAC, 25 wt% in H$_2$O), gold chloride hydrate (HAuCl$_4$, 99.995%), dimethylformamide (DMF), chloroform (CHCl$_3$, 99.9%), and tetrahydrofuran (THF, 99.9%), silver nitrate (AgNO$_3$, 99%), sodium citrate tribasic dihydrate (99%), and hydrogen peroxide (H$_2$O$_2$, 30%) were purchased from Sigma-Aldrich. Hydrochloric acid (HCl, 36%) was purchased from RCI Labscan. Ammonia solution (NH$_3$·H$_2$O, 28%) was purchased from Ajax Finechem.

Synthesis of Au NSs

NSs were synthesized using a seed-mediated method with slight modifications.[48] In the first step, 0.6 mL of 10 mM NaBH$_4$ was quickly added to a mixture of CTAB (9.9 mL, 100 mM) and HAuCl$_4$ (100 μL, 25 mM) under stirring. After 1 minute of stirring, the mixture was left undisturbed in a 30 °C water bath for 3 hours. Next, 500 μL of the resulting seeds were added to a growth solution containing L-AA (15 mL, 100 mM) and CTAC (20 mL, 200 mM), followed by the addition of 20 mL of 0.5 mM HAuCl$_4$. The solution was stirred at 300 rpm for 15 minutes and then washed twice with Milli-Q water by centrifugation at 14 500 rpm for 20 minutes. The resulting Au seeds were redispersed in 10 mL of 20 mM CTAC for further use.

In the final step, 750 μL of the CTAC-capped seeds were mixed with 20 mL of 100 mM CTAC and stirred in a 30 °C water bath. Then, 1.3 mL of 10 mM L-AA was added, followed by the injection of 20 mL of 0.5 mM HAuCl$_4$ at a rate of 20 mL h^{-1}. After the injection, the solution was stirred for an additional 10 minutes in the water bath. The resulting 25 nm Au NSs were

washed by centrifugation and redispersed in 40 mL of Milli-Q water for further use.

Synthesis of Au NCs

Au NCs were synthesized using a seed-mediated method with slight modifications.[47] A growth solution was prepared by adding 6.4 mL of 0.1 M CTAB to 32 mL of Milli-Q water, followed by the addition of 0.8 mL of 10 mM $HAuCl_4$. After introducing 4.8 mL of 0.1 M L-AA, 80 µL of CTAC-capped seeds (prepared during the NS synthesis process) was added. The resulting mixture was left undisturbed overnight in a 30 °C water bath. The final product was washed by centrifugation at 7000 rpm for 10 minutes and redispersed in 40 mL of Milli-Q water for further use.

Preparation of polymers. Thiol-terminated block copolymers were prepared by RAFT polymerization. Refer to Sections S1.1–S1.3 and Fig. S18–S25 for more details.

Synthesis of Au NRs

Au NRs were synthesized using a seed-mediated method with slight modifications.[50] The Au seed for Au NRs was synthesized by quickly injecting 600 µL of 10 mM $NaBH_4$ into a mixture of CTAB (9.9 mL, 100 mM) and $HAuCl_4$ (100 µL, 25 mM) under stirring. After 1 minute of stirring, the mixture was left undisturbed in a 30 °C water bath for 3 hours. 48 µL of the prepared Au seed was then added to the growth solution containing CTAB (39.2 mL, 0.1 M), $HAuCl_4$ (1.2 mL, 25 mM), $AgNO_3$ (800 µL, 4 mM), and L-AA (320 µL, 80 mM). After fully mixing the growth solution and the Au seed, the mixture was left undisturbed in a 30 °C water bath for 2 hours. The obtained AuNRs were washed by centrifugation at 7000 rpm for 10 minutes and redispersed in 20 mL of Milli-Q water for further use.

Synthesis of Au NBPs

Au NBPs were synthesized using a seed-mediated method with slight modifications.[50] The Au seed for Au NBPs was synthesized by quickly injecting 250 µL of 10 mM $NaBH_4$ into a mixture of Milli-Q water (10 mL), sodium citrate tribasic dihydrate (75 µL, 34 mM) and $HAuCl_4$ (100 µL, 25 mM) under stirring. After 1 minute of stirring, the mixture was left undisturbed in air for 2 hours. The growth solution of Au NBPs was prepared by mixing CTAB (100 mL, 0.1 M), $HAuCl_4$ (2 mL, 25 mM), $AgNO_3$ (1 mL, 10 mM), HCl (2 mL, 1 M), and L-AA (800 µL, 100 mM). Next, 800 µL of the prepared Au seed was added to the growth solution with fully mixing. The mixed solution was left undisturbed overnight in a 30 °C water bath. The resulting nanoparticles were washed by centrifugation at 7830 rpm for 30 minutes and redispersed in CTAC solution (70 mL, 80 mM). To purify Au NBPs, the obtained nanoparticles in CTAC solution were mixed with $AgNO_3$ (44 mL, 10 mM) and L-AA (22 mL, 100 mM) in a 60 °C water bath under stirring. After 4 hours of stirring, the mixture was cooled in air for 2 hours. The obtained nanoparticles were centrifuged at 6000 rpm for 10 minutes and redispersed in 50 mL of 50 mM CTAB solution. The colloidal solution was left undisturbed in 30 °C water bath for 4 hours, then the supernatant was removed and the

precipitate was redispersed in 25 mL of 50 mM CTAB solution. The solution was left in the 30 °C water bath again for 2 hours and then the supernatant was removed. In the final step, the precipitate was etched by the mixture of 1.2 mL of H_2O_2 and 1.2 mL of $NH_3 \cdot H_2O$. The etching process was monitored through the UV-Vis absorption spectrum of solution checked every hour. If the etching was not completed, more H_2O_2 and $NH_3 \cdot H_2O$ (200 µL + 200 µL) can be added. After the etching completed, the purified Au NBPs were washed by centrifugation at 8000 rpm for 10 minutes and redispersed in 25 mL of 50 mM CTAB for further use.

PS-*b*-P(S-*r*-AA)-SH-capped NSs. The synthesized NSs were functionalized with PS-*b*-P(S-*r*-AA)-SH *via* a two-step ligand exchange process. First, 6 mL of 25 nm NSs were centrifuged at 11 000 rpm for 10 minutes, and the supernatant was removed. The precipitated NSs were then slowly added drop-wise into 2.4 mL of PS-*b*-P(S-*r*-AA)-SH in THF under sonication. The mixture was sonicated for 40 minutes and then left undisturbed in a fume hood overnight. The PS-*b*-P(S-*r*-AA)-SH-capped NSs were subsequently washed with THF five times *via* centrifugation and finally redispersed in 3 mL of THF for further use.

PEG-*b*-P(S-*r*-DMAEMA)-SH-capped NCs. Similar to the preparation of PS-*b*-P(S-*r*-AA)-SH-capped NSs, the PEG-*b*-P(S-*r*-DMAEMA)-SH-capped NCs were prepared by centrifuging 5 mL of NCs at 7500 rpm for 10 minutes and slowly dropping the precipitate into 2 mL of PEG-*b*-P(S-*r*-DMAEMA)-SH in DMF under sonication. After sonicating for 80 minutes, the solution was left undisturbed overnight. The PEG-*b*-P(S-*r*-DMAEMA)-SH-capped NCs were then washed with THF five times by centrifugation and redispersed in 2 mL of THF for further use.

Assembly of binary molecules

The binary molecules were prepared by mixing 2 mL of PEG-*b*-P(S-*r*-DMAEMA)-SH-capped NCs with 0.6 mL of PS-*b*-P(S-*r*-AA)-SH-capped NSs. The mixed solution was sonicated for 30 minutes and left undisturbed for 2 hours. For the experiment involving the preparation of binary molecules with different NC to NS feeding ratios, the following feed volumes were used (Table 1).

For the binary molecules of NBP + NS, NBP + NC, and NR + NS, the following parameters were used (Table 2).

Assembly of binary assemblies

The binary assemblies were fabricated using a modified air–water drying-mediated method. For the slow-drying assembly,

Table 1 Summary of the feed volumes of NCs and NSs

Volume of PEG-*b*-P(S-*r*-DMAEMA)-SH NC (ml)	Volume of PS-*b*-P(S-*r*-AA)-SH NS (ml)	Theoretical number ratio of NC : NS
2	0.69	1 : 3
2	1.15	1 : 5
2	1.62	1 : 7
2	2.08	1 : 9
2	3	1 : 13

Table 2 Summary of the feed volumes of NBP, NS, NC, and NR

Au NC (0.5 mg ml^{-1} PEG-*b*-P(S-*r*-DMAEMA)-SH)	NBP (1 mg ml^{-1} PS-*b*-P(S-*r*-AA)-SH)
8 ml	0.45 ml
NBP (5 mg ml^{-1} PEG-*b*-P(S-*r*-DMAEMA)-SH)	NS (0.5 mg ml^{-1} PS-*b*-P(S-*r*-AA)-SH)
2 ml	0.7 ml
NR (5 mg ml^{-1} PEG-*b*-P(S-*r*-DMAEMA)-SH)	NS (0.5 mg ml^{-1} PS-*b*-P(S-*r*-AA)-SH)
5 ml	0.7 ml

the binary solution was centrifuged at 7500 rpm for 10 minutes and redispersed in chloroform. This chloroform-redispersed binary solution was then centrifuged again at 7500 rpm for 10 minutes. After removing the supernatant, approximately 20 μL of chloroform was retained and mixed with the binary molecules. The concentrated binary nanocrystal solution was then dropped onto the surface of a water droplet placed inside a chamber filled with chloroform. The system was covered with a glass Petri dish and left undisturbed until the water completely evaporated. For the entropy-driven assembly, the procedure was identical to that of the slow-drying method, except that the chloroform atmosphere and glass cover were omitted.

Simulation

The full-wave numerical simulations of the absorption response of the normal- and slow-drying binary plasmenes were performed using the commercially available software, CST Microwave Studio Suite®. For each assembly, a unit cell was first designed and periodic boundary conditions were implemented along the both lateral directions of the unit cell to simulate a 2D array. Plane wave excitation was used to obtain the absorption spectrum over the specified wavelength window of 350 nm to 1200 nm. To capture minute structural details of the nanoparticles, fine tetrahedral meshing with adaptive refinement was used in the simulations. Au nanoparticles in the assembly were covered with ligands and the effect of which was approximated in the permittivity of the surrounding medium (assumed to be fully covered in polystyrene). Permittivity values of Au were taken from the literature.

Characterization

The UV-Vis absorption spectra of nanocrystals and binary solutions were measured using an Agilent Cary 60 UV-Vis spectrophotometer. The UV-Vis absorption spectra of binary assemblies were measured using an Agilent Cary 6000i UV-Vis-NIR spectrophotometer. The SEM images were taken using an FEI Nova NanoSEM 430. The TEM images were taken using an FEI Tecnai F20 FEG-TEM.

Author contributions

Q. S., B. F., and W. C. designed the experiments. Q. S., B.F., and X. C. carried out the experiments, characterization studies, and data analysis. D. S. conducted the simulations. Y. H., J. Y., and Y. L. synthesized the Au nanoparticles. B. F. and S. H. T. designed and synthesized the polymers. Q. S., B. F., S. H. T., and W. C. discussed the results and co-wrote the paper.

Conflicts of interest

The authors declare that they have no known competing financial interests or personal relationships that could have appeared to influence the work reported in this paper.

Data availability

The data supporting this article have been included as part of the SI. Synthesis of copolymers (materials and methods, preparation of PS$_n$-*b*-P(S$_x$-*r*-AA$_y$)-SH), preparation of PEG$_{113}$-*b*-P(S$_{186}$-*r*-DMAEMA$_{93}$)-SH) and Fig. S1–S25. See DOI: **https://doi.org/10.1039/d5nh00381d**.

Acknowledgements

References

1 X. Ye, J. Chen, M. Eric Irrgang, M. Engel, A. Dong, S. C. Glotzer and C. B. Murray, *Nat. Mater.*, 2017, **16**, 214–219.

2 D. V. Talapin, E. V. Shevchenko, M. I. Bodnarchuk, X. Ye, J. Chen and C. B. Murray, *Nature*, 2009, **461**, 964–967.

3 A. Dong, X. Ye, J. Chen and C. B. Murray, *Nano Lett.*, 2011, **11**, 1804–1809.

4 X. Ye, C. Zhu, P. Ercius, S. N. Raja, B. He, M. R. Jones, M. R. Hauwiller, Y. Liu, T. Xu and A. P. Alivisatos, *Nat. Commun.*, 2015, **6**, 10052.

5 E. V. Shevchenko, M. Ringler, A. Schwemer, D. V. Talapin, T. A. Klar, A. L. Rogach, J. Feldmann and A. P. Alivisatos, *J. Am. Chem. Soc.*, 2008, **130**, 3274–3275.

6 E. V. Shevchenko, D. V. Talapin, N. A. Kotov, S. O'Brien and C. B. Murray, *Nature*, 2006, **439**, 55–59.

7 E. V. Shevchenko, D. V. Talapin, C. B. Murray and S. O'Brien, *J. Am. Chem. Soc.*, 2006, **128**, 3620–3637.

8 A. Dong, J. Chen, P. M. Vora, J. M. Kikkawa and C. B. Murray, *Nature*, 2010, **466**, 474–477.

9 K. J. M. Bishop, C. E. Wilmer, S. Soh and B. A. Grzybowski, *Small*, 2009, **5**, 1600–1630.

10 K. J. Si, Y. Chen, Q. Shi and W. Cheng, *Adv. Sci.*, 2018, **5**, 1700179.

11 S. J. Tan, M. J. Campolongo, D. Luo and W. Cheng, *Nat. Nanotechnol.*, 2011, **6**, 268–276.

12 L. Y. T. Chou, K. Zagorovsky and W. C. W. Chan, *Nat. Nanotechnol.*, 2014, **9**, 148–155.

13 A. Kuzyk, R. Schreiber, Z. Fan, G. Pardatscher, E.-M. Roller, A. Högele, F. C. Simmel, A. O. Govorov and T. Liedl, *Nature*, 2012, **483**, 311–314.

14 S. Pal, Z. Deng, H. Wang, S. Zou, Y. Liu and H. Yan, *J. Am. Chem. Soc.*, 2011, **133**, 17606–17609.

15 S. Simoncelli, E.-M. Roller, P. Urban, R. Schreiber, A. J. Turberfield, T. Liedl and T. Lohmüller, *ACS Nano*, 2016, **10**, 9809–9815.

16 W. Ma, H. Kuang, L. Xu, L. Ding, C. Xu, L. Wang and N. A. Kotov, *Nat. Commun.*, 2013, **4**, 2689.

17 L. Xu, S. Zhao, W. Ma, X. Wu, S. Li, H. Kuang, L. Wang and C. Xu, *Adv. Funct. Mater.*, 2016, **26**, 1602–1608.

18 G. Yao, J. Li, Q. Li, X. Chen, X. Liu, F. Wang, Z. Qu, Z. Ge, R. P. Narayanan, D. Williams, H. Pei, X. Zuo, L. Wang, H. Yan, B. L. Feringa and C. Fan, *Nat. Mater.*, 2020, **19**, 781–788.

19 T. G. W. Edwardson, K. L. Lau, D. Bousmail, C. J. Serpell and H. F. Sleiman, *Nat. Chem.*, 2016, **8**, 162–170.

20 W. Liu, P. Gupta, Y. Zhang, K. Thapa, S. Singamaneni and R. Wang, *ACS Appl. Opt. Mater.*, 2025, **3**, 514–519.

21 G. Chen, K. J. Gibson, D. Liu, H. C. Rees, J.-H. Lee, W. Xia, R. Lin, H. L. Xin, O. Gang and Y. Weizmann, *Nat. Mater.*, 2019, **18**, 169–174.

22 C. Yi, H. Liu, S. Zhang, Y. Yang, Y. Zhang, Z. Lu, E. Kumacheva and Z. Nie, *Science*, 2020, **369**, 1369–1374.

23 Z. Nie, D. Fava, E. Kumacheva, S. Zou, G. C. Walker and M. Rubinstein, *Nat. Mater.*, 2007, **6**, 609–614.

24 Z. Nie, D. Fava, M. Rubinstein and E. Kumacheva, *J. Am. Chem. Soc.*, 2008, **130**, 3683–3689.

25 Y. Cai and P. Vana, *Angew. Chem., Int. Ed.*, 2023, **62**, e202309798.

26 H. Fang, Q. Gao, Y. Rong, Y. Chen, J. Huang, H. Tong, Z. Nie, H. Tanaka, W. Li and P. Tan, *Nat. Commun.*, 2025, **16**, 2819.

27 Y. Wu, Y. Yang, Y. Zhang, L. Dai, W. Dong, H. He, H. Li, Z. Nie and Y. Sang, *Angew. Chem., Int. Ed.*, 2024, **63**, e202313406.

28 X. Shen, H. He, D. Zheng, W. Cao, Y. Sang and Z. Nie, *ACS Nano*, 2024, **18**, 20999–21008.

29 F. Lu, K. G. Yager, Y. Zhang, H. Xin and O. Gang, *Nat. Commun.*, 2015, **6**, 6912.

30 J. Kim, Q. Zhao, I. Choi, M. J. Oh, S. Kwon and S. Park, *Nat. Commun.*, 2025, **16**, 2762.

31 Z. Li, Y. Lim, I. Tanriover, W. Zhou, Y. Li, Y. Zhang, K. Aydin, S. C. Glotzer and C. A. Mirkin, *Sci. Adv.*, 2024, **10**, eadp3756.

32 D. J. Park, C. Zhang, J. C. Ku, Y. Zhou, G. C. Schatz and C. A. Mirkin, *Proc. Natl. Acad. Sci. U. S. A.*, 2015, **112**, 977–981.

33 E. Auyeung, T. I. N. G. Li, A. J. Senesi, A. L. Schmucker, B. C. Pals, M. O. de la Cruz and C. A. Mirkin, *Nature*, 2014, **505**, 73–77.

34 D. Dong, R. Fu, Q. Shi and W. Cheng, *Nat. Protoc.*, 2019, **14**, 2691–2706.

35 K. J. Si, D. Sikdar, L. W. Yap, J. K. K. Foo, P. Guo, Q. Shi, M. Premaratne and W. Cheng, *Adv. Opt. Mater.*, 2015, **3**, 1710–1717.

36 K. J. Si, P. Guo, Q. Shi and W. Cheng, *Anal. Chem.*, 2015, **87**, 5263–5269.

37 D. Dong, L. W. Yap, D. M. Smilgies, K. J. Si, Q. Shi and W. Cheng, *Nanoscale*, 2018, **10**, 5065–5071.

38 Q. Shi, D. E. Gómez, D. Dong, D. Sikdar, R. Fu, Y. Liu, Y. Zhao, D.-M. Smilgies and W. Cheng, *Adv. Mater.*, 2019, **31**, 1900989.

39 R. Fu, T. Warnakula, Q. Shi, L. W. Yap, D. Dong, Y. Liu, M. Premaratne and W. Cheng, *Nanoscale Horiz.*, 2020, **5**, 1515–1523.

40 Q. Shi, R. Fu, D. Sikdar, T. Perera, A. S. R. Chesman, Z. Yong, Y. Lu, Y. Liu, Z. Guo, S. Gong, M. Premaratne and W. Cheng, *J. Phys. Chem. C*, 2021, **125**, 27753–27762.

41 K. J. Si, D. Dong, Q. Shi, W. Zhu, M. Premaratne and W. Cheng, *Mater. Today*, 2019, **23**, 9–15.

42 S. Rao, K. J. Si, L. W. Yap, Y. Xiang and W. Cheng, *ACS Nano*, 2015, **9**, 11218–11224.

43 R. Fu, Q. Shi, Z. Yong, J. C. Griffith, L. W. Yap and W. Cheng, *Mater. Horiz.*, 2021, **8**, 259–266.

44 Z. Yong, L. W. Yap, R. Fu, Q. Shi, Z. Guo and W. Cheng, *Mater. Horiz.*, 2021, **8**, 2533–2540.

45 Y. Huang, Q. Shi, S. Liu and W. Cheng, *Adv. Funct. Mater.*, 2025, **35**, 2423869.

46 Y. Huang, Q. Shi and W. Cheng, *ACS Nano*, 2024, **18**, 29214–29222.

47 Q. Shi, D. Sikdar, R. Fu, K. J. Si, D. Dong, Y. Liu, M. Premaratne and W. Cheng, *Adv. Mater.*, 2018, **30**, 1801118.

48 F. Schulz, O. Pavelka, F. Lehmkühler, F. Westermeier, Y. Okamura, N. S. Mueller, S. Reich and H. Lange, *Nat. Commun.*, 2020, **11**, 3821.

49 K. J. Si, D. Sikdar, Y. Chen, F. Eftekhari, Z. Xu, Y. Tang, W. Xiong, P. Guo, S. Zhang, Y. Lu, Q. Bao, W. Zhu, M. Premaratne and W. Cheng, *ACS Nano*, 2014, **8**, 11086–11093.

50 Q. Shi, K. J. Si, D. Sikdar, L. W. Yap, M. Premaratne and W. Cheng, *ACS Nano*, 2016, **10**, 967–976.